Electronic Supplementary Material (ESI) for Soft Matter.

Supporting information for "Overcurvature induced multistability of linked conical frusta: How a 'bendy straw' holds its shape"

Nakul P. Bende[a], Tian Yu[b], Nicholas A. Corbin[b], Marcelo A. Dias[c], Christian D. Santangelo[d], James A. Hanna[b,e,1], and Ryan C. Hayward[a,1]

[a]Polymer Science and Engineering, University of Massachusetts Amherst, MA, USA; [b]Department of Biomedical Engineering and Mechanics, Virginia Polytechnic Institute and State University, Blacksburg, VA, USA; [c]Department of Engineering, Aarhus University, Aarhus, Denmark; [d]Department of Physics, University of Massachusetts Amherst, MA, USA; [e]Department of Physics & Center for Soft Matter and Biological Physics, Virginia Polytechnic Institute and State University, Blacksburg, VA, USA

Protocol for designing and fabricating elastic RCF :

The re-configurable conical frusta (RCF) consist of two conical frusta inverted with respect to each other, as shown in Fig.S1. A conical frustum with base radius R, height h_1 and slant angle α_1 (corresponding to an aperture angle of $\pi - 2\alpha_1$) constitutes the 'upper' frustum. Fixing the slant angle of the 'lower' frustum as $\alpha_2 = \alpha_1 + \Delta\alpha$ and the base radius R sets the cone height to $h_2 = R\tan(\alpha_2)$. The set of curves defining the mid-plane are then shifted laterally by $\pm t/2$ on either side to realize a shell with wall thickness t. Additional geometric operations necessary for fixing the shell at constant thickness t are performed (Fig.S1), by shifting the bottom-inner walls inwards {by $\tan(\alpha_1) - \tan(\alpha_2)$} and curving the inner portion of both frusta around the central region. Lastly, the shell walls are 'creased' on either end, in the form of a region around the bases with reduced thickness t_c. Thick cylinders ($t = 5$ mm) constrain the conical bases on both sides, and are held by customized grips (discussed in the following sections) during testing.

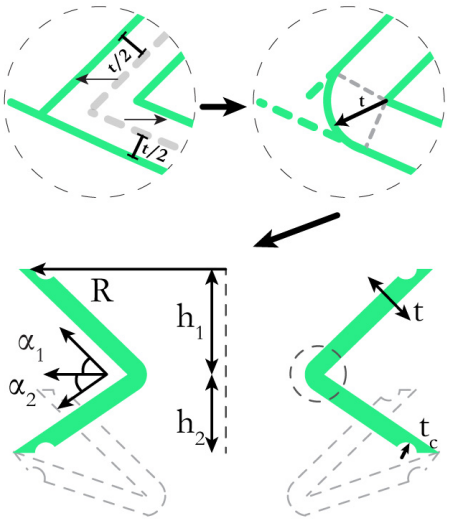

Fig. S1. RCF geometry: Series of geometric operations necessary to obtain an RCF with given parameters.

Elastic shells with intended geometries are fabricated using a two-part curable silicone elastomer, poly(vinyl siloxane) (PVS, Elite Double 32, Zhermack Inc., Italy), by resin cure molding at room temperature. Zhermack silicones are formulated for dental applications, and the minimal shrinkage due to curing produces parts with no measurable amount of pre-stress. The 4-part negative molds with appropriate geometrical parameters are modeled using a parametric 3D CAD algorithm (Grasshopper plug-in, Rhino, Robert McNeel Inc., USA) (Fig.S2A). The molds are printed with poly(acrylonitrile-butadiene-styrene) using a commercial 3D printer (Dimension uPrint SE Plus, Stratasys, USA) as shown in Fig.S2B.

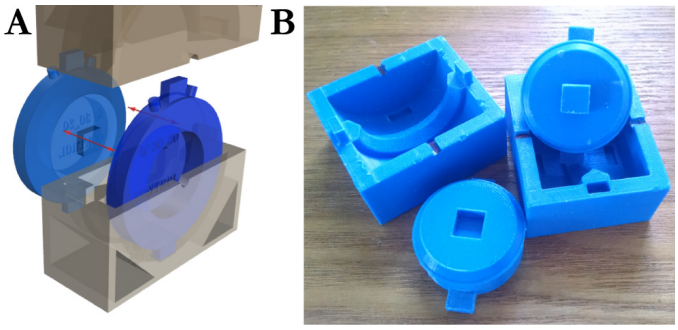

Fig. S2. (A) CAD model, with indicated assembly for 4-part molds. **(B)** 3D printed negative molds used for fabricating RCF with a room temperature resin-cure molding of poly(vinyl siloxane) elastomer.

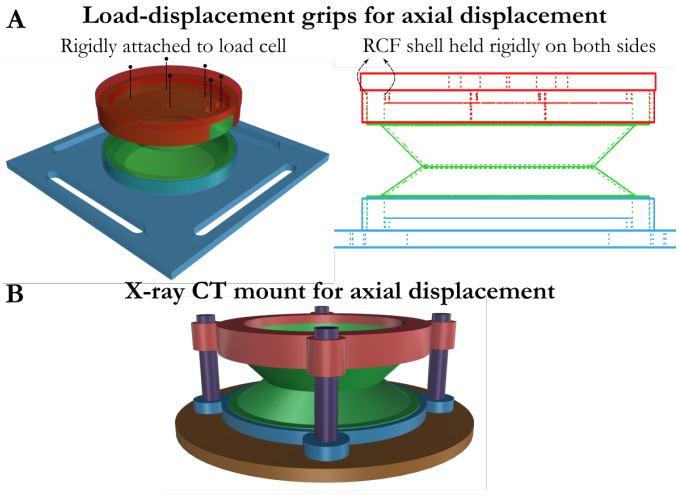

Fig. S3. Customized mount for a controlled axial deformation of RCF for load-displacement setup **(A)** and X-ray CT setup **(B)**. The upper grip is slid on pegs to impart controlled axial deformation between X-ray CT scans. 3D CAD models indicate the manner in which grips provide rigid boundary conditions to the shell.

To cast an RCF geometry, a mold release agent (MR311, Sprayon, Canada) is first applied to 3D printed molds. A 1:1 (prepolymer:crosslinker) mixture of the PVS ingredients is introduced into the mold, followed by immediate degassing under vacuum for 8-10

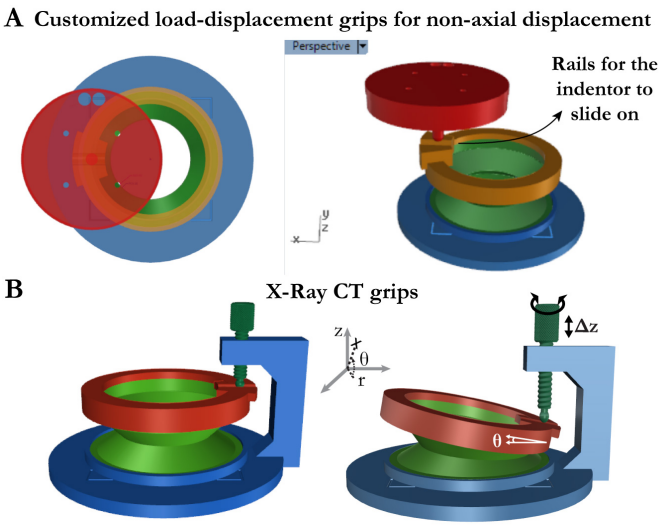

Fig. S4. Customized indenter-grip combination for a controlled non-axial deformation of RCF for load-displacement setup **(A)** and X-ray CT setup **(B)**. 3D CAD models indicate the railings along which the indenter can slide freely, converting a linear translation in the z direction to a controlled tilt angle θ.

minutes to remove any air bubbles. The molds are assembled as shown in Fig.S2A, and held under room temperature for 30 minutes while curing. Finally, the molds are opened carefully and excess elastomer is removed from the final cured RCF . Samples with bubbles, irregular thickness or other defects are discarded. This method proves to be fairly robust, resulting in shells with $t = 0.5 \pm 0.05$ mm.

Custom mounts for axial deformation

During load-displacement measurements, an RCF is held rigidly in custom designed grips to aid in alignment and impart strict boundary conditions. The thick cylinders on either side of the RCF (Fig.S3A) rigidly constrain both conical bases during deformation. Similarly, to impart axial deformation during X-ray CT scanning, the mount is modified to include a sliding mechanism for the upper grip (Fig.S3B).

Custom mounts for non-axial deformation

Imparting a controlled non-axial deformation to the RCF geometry poses a considerable challenge, as the point of contact travels in a curvilinear path. Limited by the ability to control only the linear translation of the indenter, a custom indenter-grip is designed for converting this linear translation in z direction to non-axial tilt. As shown in Fig.S4, a linearly translated indenter pushes on customized grips that hold the sample. At the point of contact, these grips consist of a smooth railing, allowing the indenter to slide in the lateral direction

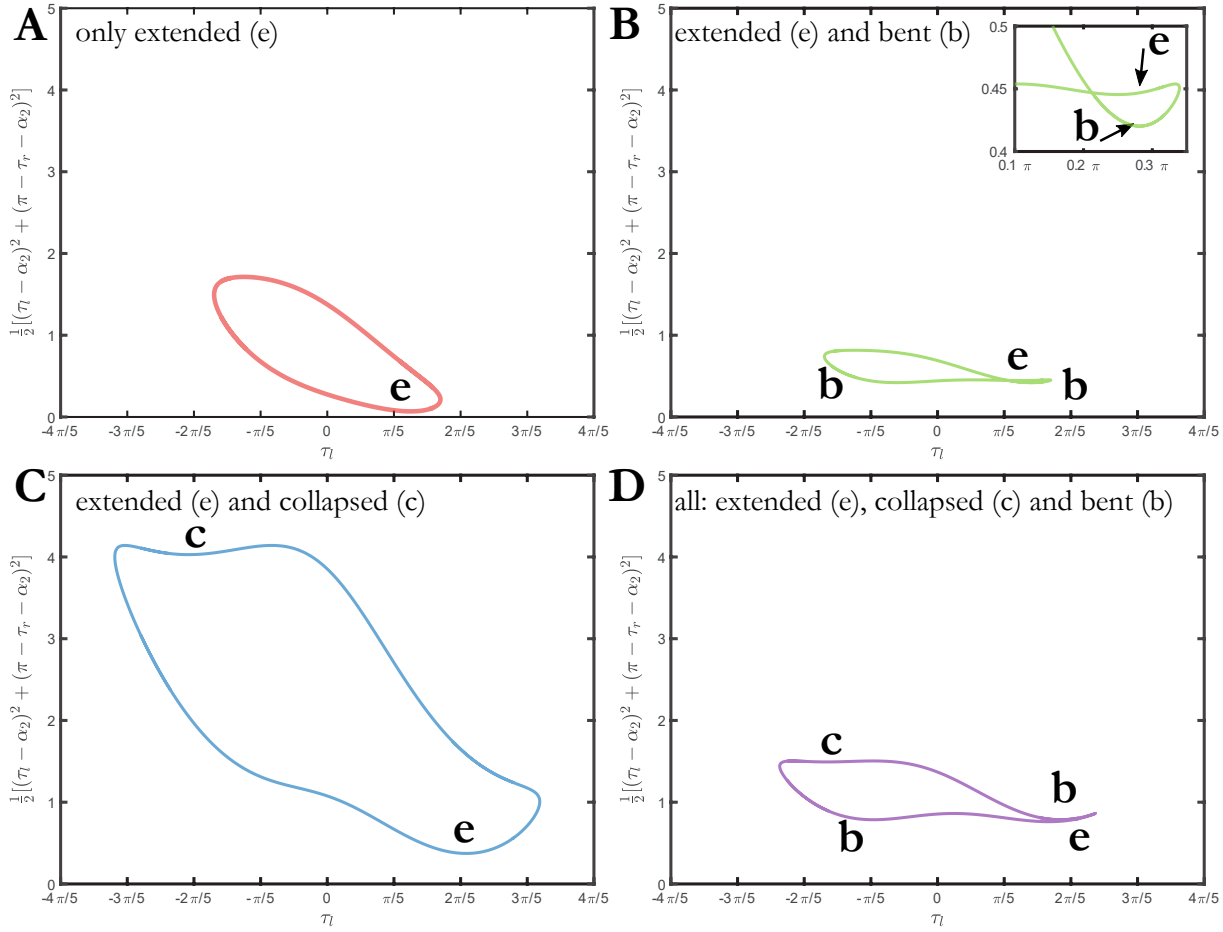

Fig. S5. Energy landscapes for incompatible 4-bar linkage and torsional spring model. The curves correspond to samples with different geometrical parameters (cone angle: α_2 and mismatch: $\beta - \alpha_2$) described in Fig.5 (main text).

(r), converting the linear translation along the z axis of the point indenter into a controlled non-axial tilt angle θ.

Four bar linkage model

We further describe the 4-bar linkage model constructed as in the main text, Fig.5. We can write the Lagrangian of this configuration as,

$$\begin{aligned}\mathcal{L} =& \frac{1}{2}K_r(\tau_l-\alpha_2)^2+\frac{1}{2}K_r(\pi-\tau_r-\alpha_2)^2+\\ &\lambda[(2R+W\cos\tau_r-W\cos\tau_l)^2+(W\sin\tau_r-W\sin\tau_l)^2\\ &-(2R-2W\cos\beta)^2] \qquad \text{[S1]}\end{aligned}$$

where the last term quadratically enforces the constraint that the two ends of the crank links without any springs are the same distance apart as the floating bar length. Upon variation of the angles τ_l and τ_r, the resulting Euler-Lagrange equations are,

$$K_r(\tau_l-\alpha_2)+2\lambda[2RW\sin\tau_l+W^2\sin(\tau_l-\tau_r)]=0 \qquad \text{[S2]}$$

$$K_r(\tau_r+\alpha_2-\pi)+2\lambda[-2RW\sin\tau_r+W^2\sin(\tau_r-\tau_l)]=0 \qquad \text{[S3]}$$

Eq.S2 and Eq.S3 can be combined to eliminate the multiplier λ. Dividing out the only modulus K_r leaves us with one equilibrium equation and one constraint equation,

$$\begin{aligned}&(\tau_l-\alpha_2)(W\sin(\tau_r-\tau_l)-2R\sin(\tau_r))+\\ &(\tau_r-\pi+\alpha_2)(W\sin(\tau_r-\tau_l)-2R\sin\tau_l)=0 \qquad \text{[S4]}\\ &(2R+W\cos\tau_r-W\cos\tau_l)^2+(W\sin\tau_r-W\sin\tau_l)^2-\\ &(2R-2W\cos\beta)^2=0 \qquad \text{[S5]}\end{aligned}$$

We numerically continue equilibria of these equations along deformation paths using AUTO 07P (1). The behavior of the total energy of the system along these curves provides stability information.

Fig.S5 shows 4 closed curves corresponding to the energies of states represented by dots in Fig.5 (main text), with one link angle τ_l as parameter. For all of these curves, state *(e)*, analogous to the extended state of a straw, is always a minimum on the lower right, but not always the ground state. Two equivalent-energy bent states *(b)* appear on the green curve, where they are the ground states, and on the purple curve, where they are a little bit higher energy than the *(e)* state. On all curves, the fully inverted axially symmetric state *(c)*, analogous to the collapsed state of a straw, is on the upper left. It is a maximum for the green and red curves and a minimum for the blue and purple curves.

We can move from the red to the green curve by decreasing the original cone angle α_2 and increasing the mismatch $\beta-\alpha_2$, creating the two partially inverted local minima *(b)*. From here we can create the collapsed local minimum *(c)* by either further increasing the mismatch to move to the purple curve, or increasing the original cone angle to move to the blue curve; in the latter case, we lose the partially inverted states. As can be seen from Fig.5 (main text), simply increasing mismatch at fixed original cone angle will eventually stabilize all the available states, but the order in which this happens depends on the original cone angle.

Understanding deformation of RCF through curvature analysis

Curvature measurement by in-situ X-ray CT:
A Perkin Elmer IVIS SpectrumCT imager is used to obtain X-ray computed tomograms by exposing samples at a 23 mGy dose through a 120-mil-thick copper foil filter. The resulting scans (voxel size 150 μm) are thresholded accordingly in ImageJ for generating a 3D image stack for the desired geometry. To avoid possible interference during curvature measurement, the outer and inner surfaces of shell are separately identified using MATLAB (Mathworks Inc., USA), and a 3D point cloud depicting the inner surface is exported to the Meshlab software package (2). Therein, following a reduction of dense point clouds (3), surface curvatures are computed using the algebraic point

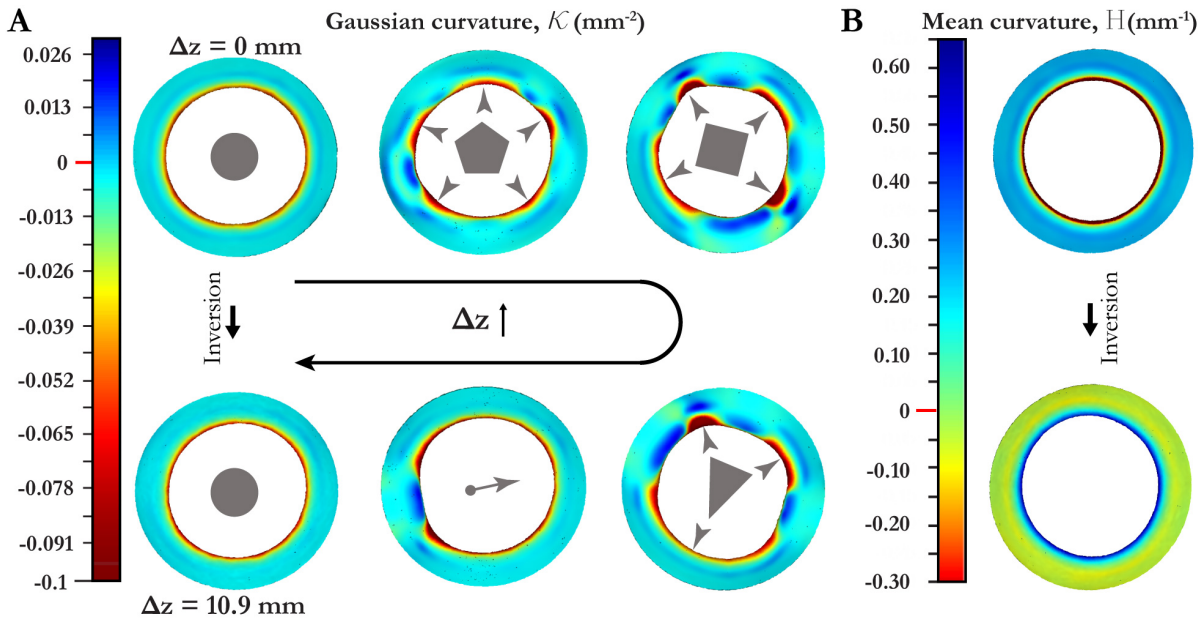

Fig. S6. Distribution of Gaussian ($\mathcal{K}$) and mean (H) curvature during axial deformation of RCF with $h_1 = 10$ mm, $\alpha_1 = 45^o$ and $O = 0^o$: **(A)** Measured Gaussian curvature ($\mathcal{K}$) from X-ray computed tomography data, for axial indentation depths Δz. After an initial axisymmetric deformation regime, we observe periodic buckling of the central region upon axial indentation characterized with an initial mode of $m = 5$ at $\Delta z = 2.9$ mm, gradually depleting due to merging 'crest' regions at $\Delta z = 7.9$ mm ($m = 4$), 8.9 mm ($m = 3$) and 10.8 mm ($m = 2$), before regaining an axisymmetry in the isometric state at $\Delta z = 10.9$ mm. As clearly seen in color-maps, a majority of Gaussian curvature is concentrated in the central buckled region. **(B)** Measured mean curvature H of isometric states at $\Delta z = 0$ and 10.9 mm.

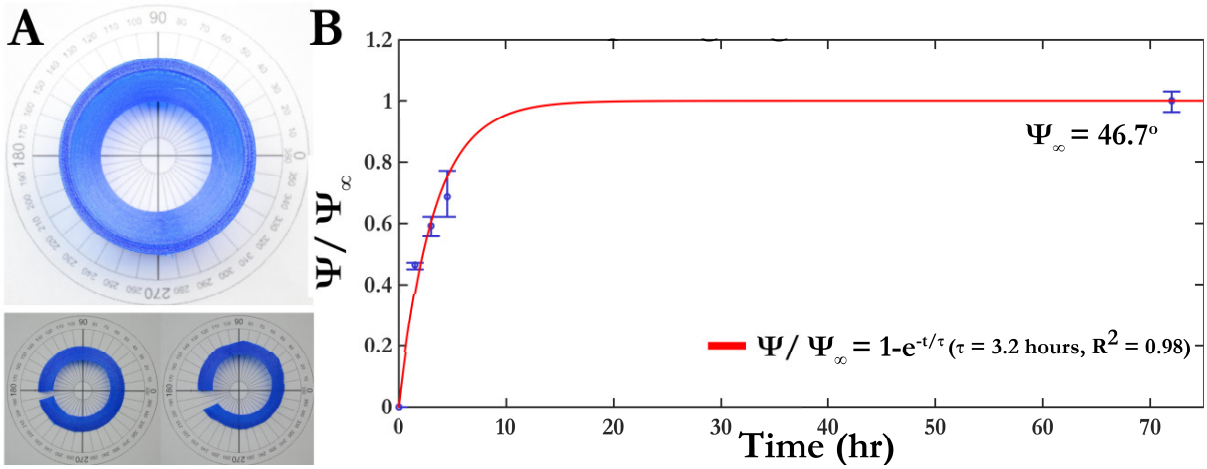

Fig. S7. Opening angle ψ (as proxy of overcurvature) of 3D printed RCF as a function of time spent in an axially collapsed state.

set surface method (4).

Curvature measurement during axial deformation of RCF : Curvature evolution during axial deformation is measured for RCF ($h_1 = 10$ mm, $\alpha_1 = 45^o$ and $O = 0^o$) indenting the shell quasi-statically with a step size of < 1 mm. $\mathcal{K}$ is superimposed on the deformed geometries at various Δz for analysis in Fig.S6A as seen from below. At $\Delta z = 0$, an expected $\mathcal{K} = 0$ is observed except in the central region, where $\mathcal{K} < 0$. Upon further indentation, breaking of axisymmetry is observed, similar to the load-displacement experiments. As marked in Fig.S6A, this buckled region appears to be periodic at $\Delta z = 2.9$ mm, characterized by a periodicity $m = 5$. Proceeding through the next steps of indentation at $\Delta z = 4$, 8.9 and 10.8 mm, we consistently note two 'crest' regions merging into one, changing the mode from $m = 5$, to $m = 4$, 3 and 2 along the each step. A stable full inversion of the lower frustum restores axial symmetry and distribution of $\mathcal{K}$ at $\Delta z = 10.9$ mm. H of isometric states ($\Delta z = 0$ and 10.9) is also plotted in Fig.S6B, demonstrating the expected inversion in sign.

Quantifying overcurvature introduced in 3D printed RCF

Controlled amounts of overcurvature in RCF fabricated through direct 3D printing of poly(urethane) can be introduced as follows. After being printed in an extended state, the RCF are transferred into a harness that holds the structure in an axially collapsed position for extended periods of time. After time t, samples are removed from the harness, examined for multistability and cut open. Similar to *Pop toobs*, the 3D printed RCF also open radially upon relaxation (Fig.S7). We measure the opening angle ψ, and repeat this experiment for samples that are constrained for different time periods (t). Fig.S7B shows the dependence of opening angle normalized by the value at $t = 72$ (ψ_∞), along with a one-parameter exponential fit. For the poly(urethane) in this study, keeping RCF ($h_1 = 10$ mm, $\alpha_1 = 45^o$) in collapsed state for approximately 3 hours is enough to induce sufficient overcurvature for stability of the bent state, closely matching the time-scale over which pre-stress is developed in Fig. S7B.

Bibliography

1. Doedel EJ, et al. (2007) AUTO-07P: Continuation and bifurcation software for ordinary differential equations (`indy.cs.concordia.ca/auto/`).
2. Cignoni P, et al. (2008) Meshlab: an open-source mesh processing tool. in *Eurographics Italian Chapter Conference*. Vol. 2008, pp. 129–136.
3. Corsini M, Cignoni P, Scopigno R (2012) Efficient and flexible sampling with blue noise properties of triangular meshes. *IEEE Transactions on Visualization and Computer Graphics* 18(6):914–924.
4. Guennebaud G, Gross M (2007) Algebraic point set surfaces in *ACM Transactions on Graphics (TOG)*. (ACM), Vol. 26, p. 23.

Supporting Movies

Movie M1. Load-displacement curves and corresponding images showing deformation of RCF under axial loading. Samples lacking ($h_1 = 6$ mm), and exhibiting ($h_1 = 10$ mm) axial bistability are shown.

Movie M2. Load-displacement curves and corresponding images showing axial deformation of a *Pop Toob* with its natural curvature, exhibiting smooth accordian-like deformation, and in the overcurved state, exhibiting multistability.

Movie M3. Load-displacement curves and corresponding images showing non-axial deformation of control ($O = 0$) and overcurved ($O = 0.17$) RCF with $h_1 = 6$ mm, $\alpha_1 = 45^o$ and $\alpha_2 = 35^o$. The control sample lacks stability in the bent state and shows a smaller number and amplitude of wrinkles in the transition state.

Movie M4. A *Pop Toob* kept in an extended state for approximately 1-2 days lacks pre-stress and is no longer multistable.

Movie M5. Video showing axial and non-axial loading of 3D printed RCF , revealing a change in stability due to the introduction of overcurvature.